

Asymmetric interaction of a solar wind reconnecting current sheet and its magnetic hole with Earth's bow shock and magnetopause

Hadi Madanian^{1,2}, Terry Z. Liu³, Tai D. Phan⁴, Karlheinz J. Trattner¹, Tomas Karlsson⁵, Michael W. Liemohn⁶

¹Laboratory for Atmospheric and Space Physics, University of Colorado, Boulder, CO, USA

²Space Science and Engineering Division, Southwest Research Institute, San Antonio, TX, USA

³University of California Los Angeles, Los Angeles, CA, USA

⁴Space Sciences Laboratory, University of California, Berkeley, CA, USA

⁵KTH Royal Institute of Technology, Stockholm, Sweden

⁶Department of Climate and Space Sciences and Engineering, University of Michigan, Ann Arbor, MI, USA

Key Points:

- Asymmetric interaction is caused by the current sheet plane orientation in the solar wind and foreshock effects.
- Flux of accelerated electrons and ions increase in the magnetosheath due to current sheet and magnetic hole interactions at the bow shock.
- The structure causes deformation of the bow shock and magnetopause boundaries and modulates the reconnection process at the magnetopause.

Corresponding author: Hadi Madanian, hmadanian@gmail.com

This is the author manuscript accepted for publication and has undergone full peer review but has not been through the copyediting, typesetting, pagination and proofreading process, which may lead to differences between this version and the [Version of Record](#). Please cite this article as [doi: 10.1029/2021JA030079](https://doi.org/10.1029/2021JA030079).

This article is protected by copyright. All rights reserved.

Abstract

We report results of our multi-spacecraft analysis of a solar wind reconnecting current sheet (RCS) and its solar wind magnetic hole (SWMH) observed on 20 November 2018. In the solar wind, the normal vector to the current sheet plane makes an angle of 32° with the Sun-Earth line. A combination of tilted current sheet plane and foreshock effects cause an asymmetric interaction with the bow shock, in which the structure arrives at the quasi-perpendicular side of the bow shock before the quasi-parallel side. The magnetic field strength inside the magnetic hole decreases by ~ 69 percent in the solar wind, with a similar depression rate observed inside the magnetosheath due to this structure. The solar wind flow slowdown and deflection during the bow shock crossing significantly disrupt the reconnection exhausts within the RCS. The interaction of the RCS and SWMH with the bow shock creates enhanced fluxes of accelerated electrons and ions. Plasma flow deflection in the magnetosheath also increases with the passage of the RCS. The ion density and temperature both increase within the current sheet to form a roughly pressure balanced structure. Field rotation and change in the dynamic pressure during this event modify the reconnection zones at the magnetopause and cause asymmetric inward motions in portions of the bow shock and the magnetopause boundaries (i.e., deformation). Unlike localized magnetosheath jets, an RCS and its associated SWMH in the solar wind have a global impact on the bow shock and the magnetopause.

Plain Language Summary

Space Weather is the study of effects of solar inputs on the space environment surrounding Earth. A source of solar input is through the solar wind, a stream of charged particles from the Sun carrying the interplanetary magnetic field. In this study, we analyze effects of a particular type of solar wind anomaly on Earth. The structure is initially observed by solar wind monitors far upstream of Earth, and later appears in the data of several near Earth spacecraft. We show that the structure can pass through the outer most boundary around Earth, the bow shock, and propagate closer to Earth. This study has significance in shaping our understanding of space weather as it describes near-Earth effects of a commonly observed solar wind phenomenon.

1 Introduction

Reconnection has been widely studied and observed in various space plasma environments such as solar flares, the solar wind, Earth's magnetotail and magnetopause (Gosling, 2012; Paschmann et al., 2013; Hesse & Cassak, 2020; Khotyaintsev et al., 2019; Treumann & Baumjohann, 2013; Yamada et al., 2010; Zweibel & Yamada, 2016, & references therein). During reconnection, the magnetic field morphology at the intersection of two rather different plasma environments change in order to diffuse the energy of opposing flows. In the solar wind, a reconnecting current sheet (RCS) is characterized by a rotation in the IMF accompanied by Alfvénic accelerated plasma flows also known as reconnection exhausts (Gosling et al., 2005). Alfvénic disturbances generated during reconnection propagate along reconnected magnetic field lines and accelerate and heat the plasma along their way. For a spacecraft that is relatively stationary in the supersonic solar wind flow, such a structure will appear as correlated changes in the magnetic field (\mathbf{B}) and the plasma velocity (\mathbf{V}) on one side, and anti-correlated changes on the other side of the reconnection exhaust. The current sheet can appear as back-to-back rotational discontinuities (i.e., a bifurcated current sheet) or as a single current sheet (Phan et al., 2006; Gosling & Szabo, 2008; Phan et al., 2009). The physical processes that initiate reconnection are not well determined. A few models describe the scaling relation between plasma parameters during reconnection (Cassak & Shay, 2007; Petschek, 1964; Parker, 1957). Theoretical studies suggest that in the solar wind, compression of the sectored solar wind flow can lead to reconnection (Drake et al., 2017). Reconnection can also be

70 initiated spontaneously. Transfer of magnetic energy to particles creates a magnetic de-
71 pression or a magnetic hole at the reconnection site. The level of depression varies with
72 distance to the X-line of an expanding exhaust. Energy release during reconnection is
73 also a source of free energy that drives further plasma instabilities causing turbulence
74 in the magnetic field and plasma flow near the reconnection zone (Osman et al., 2014).

75 Interaction of transient solar wind structures with Earth's bow shock and magne-
76 tosphere has been the topic of many investigations. It has been shown that sudden changes
77 in the IMF direction across rotational discontinuities (RDs) can alter the energy input
78 and reconnection rate at the magnetopause, and modify the solar wind - magnetosphere
79 - ionosphere coupling (Andreeva et al., 2011; Liemohn & Welling, 2016; Tsurutani et
80 al., 2011). Archer et al. (2012) showed that some RDs travel in the magnetosheath in
81 the form of pressure pulsations. Change of shock geometry from quasi-perpendicular to
82 quasi-parallel allows for high-pressure plasma parcels to form at certain regions down-
83 stream of the shock. Conventionally, magnetosheath "high-speed" jets are known to have
84 a characteristically high velocity component along the magnetopause normal vector that
85 gives rise to the enhanced dynamic pressure (Escoubet et al., 2020; Hietala & Plaschke,
86 2013; Plaschke et al., 2013). However, high plasma density anomalies in the magnetosheath
87 can also produce high dynamic pressure magnetosheath structures (Blanco-Cano et al.,
88 2020). It has also been shown that compression of the current sheet across solar wind
89 discontinuities at the bow shock can initiate reconnection (Lin, 1997; Phan et al., 2007;
90 Hamrin et al., 2019), as does the compression of current sheets at the magnetopause (Hietala
91 et al., 2018). Current sheet thinning, high magnetic shear angle, and small difference in
92 plasma β between the two plasma environments are favorable conditions for reconnec-
93 tion (Paschmann et al., 1982; Phan et al., 2010).

94 Bow shock and foreshock environments also significantly modify the current den-
95 sity within RDs (Kropotina et al., 2021). Crossing the bow shock can disrupt the recon-
96 nection exhausts and shut off the reconnection process within the RCS (Phan et al., 2011).
97 In some cases, density increase within upstream discontinuities generates a fast shock
98 that propagates in front of the discontinuity in the magnetosheath (Maynard et al., 2008).
99 Due to pressure variations and rarefaction effects, interplanetary shocks induce a rock-
100 ing motion in the bow shock layer when they cross it (Šafránková et al., 2007). Once in-
101 side the magnetosheath, interplanetary shocks take the form of a discontinuity (Zhang
102 et al., 2009). Bow shock crossing also significantly modifies the structure of magnetic clouds,
103 plasma events associated with interplanetary coronal mass ejections and characterized
104 by enhancements in the magnetic field strength during slow field rotations (Farrugia et
105 al., 1995; Turc et al., 2016). Another widely observed transient solar wind phenomenon
106 are magnetic holes (MHs) (Turner et al., 1977), characterized as sudden decreases in the
107 magnetic field strength in an otherwise unperturbed solar wind flow. Depending on the
108 level of magnetic field rotation across the depression, solar wind magnetic holes (SWMHs)
109 are typically classified as linear or rotational holes (Turner et al., 1977; Volwerk et al.,
110 2021). These pressure-balanced structures have been observed at various heliocentric dis-
111 tances and plasma environments and can appear in different sizes (Burlaga et al., 1990;
112 Karlsson et al., 2021; Madanian et al., 2020; Sperveslage et al., 2000; Wang et al., 2020).
113 SWMHs can bypass the bow shock almost intact and appear in the magnetosheath plasma
114 as a high momentum plasma parcel (Karlsson et al., 2015, 2016). Generation mechanism
115 of MHs has been a point of debate (Tsurutani et al., 2011). Several studies have deter-
116 mined that linear holes are associated with mirror mode waves in high beta plasmas (Burlaga
117 et al., 2007; Balikhin et al., 2012; Volwerk et al., 2021). However, a consistent process
118 for generation of rotational holes has not been identified.

119 In this paper we analyze the interaction of an RCS and its associated SWMH with
120 Earth's bow shock and magnetopause using a combination of multi spacecraft observa-
121 tions and a convection model. Given the relatively high occurrence rate of RCSs, it is
122 important to have a better understanding of their impacts on plasma boundaries around

123 Earth. In Section 2, details of observations at several plasma boundaries and environ-
 124 nments are shown. Discussions of results are provided in Section 3, and the paper is con-
 125 cluded in Section 4.

126 2 Observations

127 We use data from the Advanced Composition Analyzer (ACE) (Stone et al., 1998),
 128 Wind (Harten & Clark, 1995), Cluster (Escoubet et al., 2001), Time History of Events
 129 and Macroscale Interactions during Substorms (THEMIS) (Angelopoulos, 2008), and the
 130 Magnetospheric Multiscale (MMS) (Burch et al., 2016) missions. For the Cluster con-
 131 stellations, plasma data are only available from Cluster4 during the event studied here.
 132 Also, Cluster3 and 4 spacecraft travel very similar orbits and make nearly identical mea-
 133 surements. As such, Cluster3 data will not be discussed. Similarly, the four MMS space-
 134 craft are in a close tetrahedron formation (less than 25 km intra-spacecraft separation)
 135 during this event. We only use data from satellite 1 (MMS1). The spatial scale of the
 136 structure analyzed in this study is much larger than the MMS spacecraft separation, and
 137 kinetic-scale differences in observations of different MMS spacecraft are not considered.
 138 Positioning of these spacecraft on the dayside provide an opportunity for thorough anal-
 139 ysis of the RCS interaction with Earth's bow shock and the magnetopause. All vector
 140 quantities in the paper are expressed in the geocentric solar magnetic (GSM) coordinate
 141 system in which the x -axis points towards the Sun, the y -axis is perpendicular to Earth's
 142 magnetic dipole axis, and z completes the right-hand triple.

143 2.1 RCS in the solar wind

144 The RCS is initially observed by two solar wind monitors at Lagrange point 1. Fig-
 145 ures 1a and b show the IMF profile measured by ACE and Wind spacecraft, respectively,
 146 for a time interval between 07:50:00 and 09:30:00 UT on 20 November 2018. The ACE
 147 spacecraft is at (239.1, -15.9, 26.5) R_E ($R_E =$ Earth radius), while the Wind spacecraft
 148 is downstream from ACE at (195.7, -29.2, 7.7) R_E . Comparing the two time series, there
 149 are a few magnetic depressions at the beginning of the interval in ACE data which seem
 150 to have been replenished during the transport to Wind. We focus on the magnetic hole
 151 structure in the middle of the interval in Figure 1a between 08:31:28 and 08:35:24 UT.
 152 Throughout this paper, we consider the field rotation/reversal due to the RCS occur-
 153 ring throughout the entire SWMH period as a single structure and refer to it as the "struc-
 154 ture" or the RCS. Once the SWMH crosses the bow shock, we refer to the associated mag-
 155 netic depression in the magnetosheath as MH. The magnetic field depression ratio is de-
 156 fined as $\delta B = |B_{in} - B_{out}|/B_{out}$, where B_{in} and B_{out} are the average field strength
 157 inside and outside the SWMH, respectively. ACE measures a δB of 0.50 for this struc-
 158 ture. A very similar and comparable depression ratio of 0.69 is seen in Wind data be-
 159 tween 08:39:14 and 08:48:25 UT, corresponding to the same structure transported by the
 160 solar wind. However, at times the magnetic field strength inside the SWMH drops to lower
 161 values in Wind data compared to ACE.

162 The magnetic field and bulk plasma flow velocity components for the highlighted
 163 sub-interval are shown in Figure 1c–e. The data are from the Wind spacecraft. The ver-
 164 tical dashed lines mark the boundaries of the structure which in different plasma envi-
 165 ronments is recognized by simultaneous observations of a rotation in the magnetic field,
 166 accompanied by a decrease in the magnetic field strength, and an enhancement of the
 167 plasma density. The first vertical dashed line is drawn at t_i (the time at the leading edge)
 168 selected at the beginning of the field rotation, while the second vertical dashed line is
 169 drawn at t_f (the time at the trailing edge) determined when the magnetic field strength
 170 returns to values before t_i . In Figure 1 however, different components of the magnetic
 171 field approach the post current sheet values at different rates. By 08:47:54 UT, the field
 172 strength (dominated by B_y) has mostly reached the IMF strength in the pristine solar

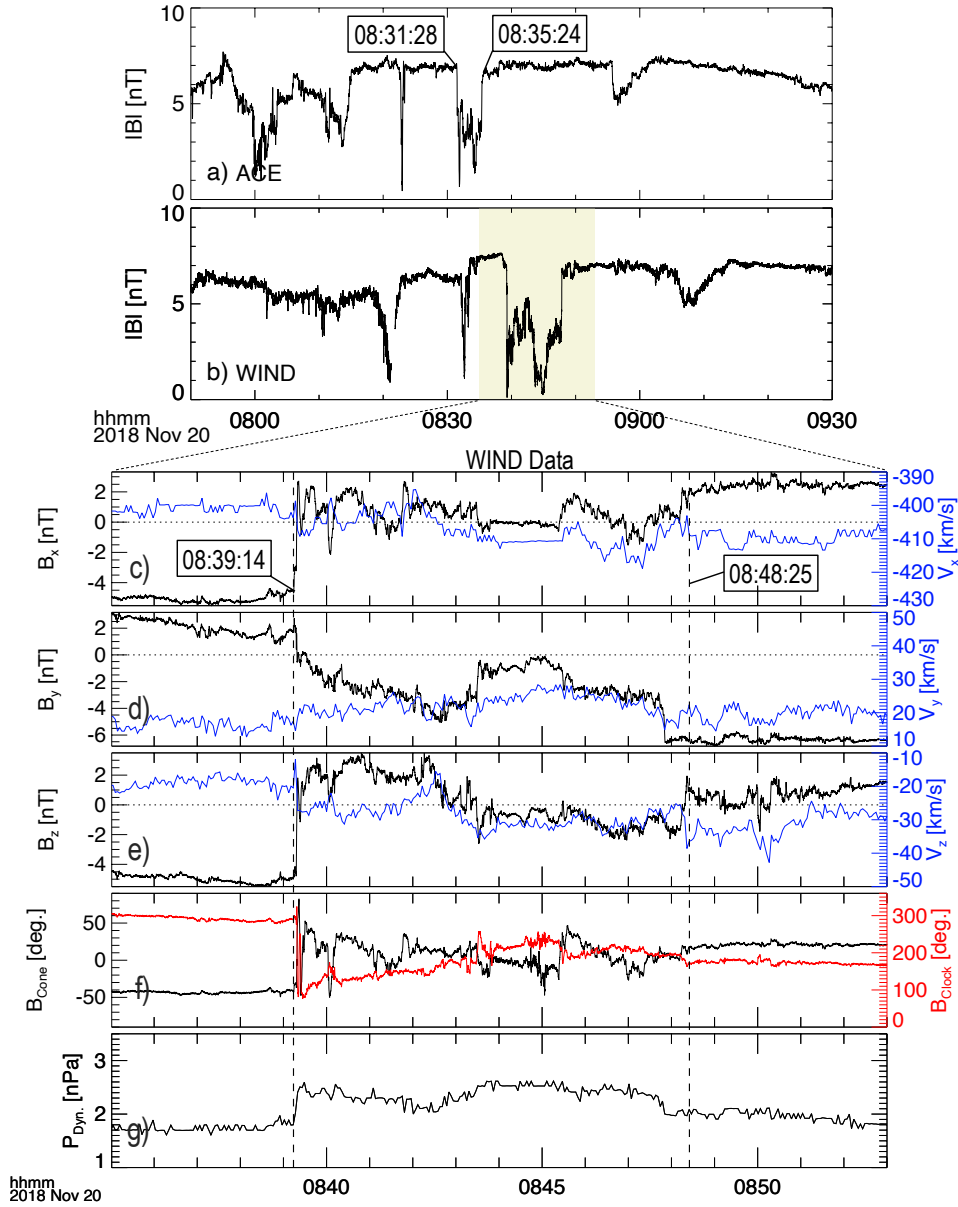


Figure 1. Solar wind magnetic field, flow velocity, and dynamic pressure for an RCS on 20 November 2018. Panels (a) and (b) show the IMF strength measured by ACE and Wind spacecraft, respectively. Panels (c–e) show GSM components of the magnetic field in black and the flow velocity in blue measured by Wind for the highlighted interval in (b). Panel (f) shows the magnetic field clock angle in red and the cone angle in black, and the dynamic pressure is shown in (g). The RCS and its SWMH boundaries (t_i and t_f) are marked with time tags in ACE data in panel (a), and with vertical dashed lines in Wind data in panels (c–g).

173 wind flow before t_i . But B_z reversal is still occurring. As such, we select t_f a few sec-
 174 onds later at 08:48:25 UT when the field rotation has completed in all three components.
 175 Similar conditions exist on the leading edge of the structure in observations near the bow
 176 shock and inside the magnetosheath. For these cases, we identify t_i when the clock
 177 angle reaches its minimum value inside the MH.

178 The magnetic field rotation is evident in the cone ($\arcsin(B_x/|B|)$) and clock ($\arctan(B_z, B_y)$)
 179 angles in Figure 1f. A cone angle of 0° indicates an IMF vector in the plane perpendic-
 180 ular to the Sun–Earth line. In that plane, the clock angle is measured from the $+y$ -axis
 181 and varies in the $0 - 2\pi$ range. Before the crossing of the current sheet, the IMF has
 182 a cone angle -42° and a clock angle of 289° . Immediately after the field rotation at 08:39:12
 183 UT, the cone and clock angles change to 35° and 126° , respectively. At the trailing edge,
 184 the cone angle approaches 20° and the clock angle reaches 176° . The magnetic shear an-
 185 gle (α) across the structure is 119.6° at ACE and reduces to 118° at Wind.

186 The structure also appears to be bifurcated, as commonly observed in solar wind
 187 RCSs (Mistry et al., 2015), with field components plateaued near its center. We also ob-
 188 serve both correlated and anti-correlated changes in \mathbf{V} and \mathbf{B} , which are best seen along
 189 the y component in Figure 1d. Subtle changes in the flow velocity (~ 15 km/s from the
 190 background solar wind) are most likely due to the reconnection exhaust. There are also
 191 velocity variations in the x and z components. The local Alfvén speed ($v_A = |\mathbf{B}|/\sqrt{\mu_0\rho}$
 192 where ρ is the plasma mass density and μ_0 is the vacuum permeability) on average is
 193 relatively low (~ 22 km/s) throughout the period which limits the outflow speed of ex-
 194 haust jets. Figure 1g shows an increase in the solar wind dynamic pressure between the
 195 vertical dashed lines. The dynamic pressure is in principle a tensor that relates the pres-
 196 sure tensor in the plasma rest frame to that measured in another frame moving with the
 197 bulk plasma flow speed. In the solar wind, the tensor element associated with the ra-
 198 dial flow component dominates all other values in the tensor and the dynamic pressure
 199 is determined from $P_{dyn.} = \rho v^2$, where v is the flow speed. Inside the SWMH, the plasma
 200 density increases from 6.4 to 8.5 cm^{-3} and the plasma temperature rises from 7.7 to 12.4
 201 eV. These observations are consistent with an extended RCS in the solar wind (Gosling
 202 et al., 2005). At the same time, these variations are unlikely to be associated with he-
 203 liospheric current sheet (HCS) crossings, as characteristic changes in pitch angle distri-
 204 bution of strahl electrons intrinsic to HCS crossings are not observed (Kahler & Lin, 1994;
 205 Kahler et al., 1998).

206 The event duration increases from 236 s at ACE to 551 s at Wind. This expansion
 207 suggests that either dynamic plasma processes within the structure have caused expan-
 208 sion of the current sheet thickness, or different spacecraft are at different distances to
 209 the X-line of an expanding exhaust. Nevertheless, the RCS and its SWMH are a mag-
 210 netohydrodynamic (MHD) scale structure. The normal vector to the RCS plane obtained
 211 from the minimum variance analysis (MVA) of the Wind magnetic field data is $n_{cs} =$
 212 $(-0.84, -0.26, 0.45)$. The normal vector at ACE deviates from this vector by less than
 213 8° . This difference could be due to rotation of the plane phase, or uncertainties associ-
 214 ated with applying the MVA. Nonetheless, the large ratio of intermediate to minimum
 215 eigenvalues of the variation matrix (see the Supplementary Information section), and small
 216 field variations along the minimum variance direction suggest that the MVA results are
 217 reliable and the normal vector is determined reasonably well. Figure S1 in Supplemen-
 218 tary Information shows more details of our MVA analysis.

219 ACE and Wind spacecraft are $\sim 50 R_E$ apart during this event, mostly along the
 220 Sun–Earth line. Spacecraft positions are listed in Table 1. Based on the solar wind bulk
 221 flow velocity and the RCS normal vector, the expected travel time between the two space-
 222 craft is 420 s, that is within 10% of the time lag (466 s) of observing the leading edge
 223 of the RCS (see Table 1). Distinct change in the clock angle accompanied by reduced
 224 magnetic field strength and increased plasma density and dynamic pressure are features
 225 that enable distinguishing and tracking the structure through different plasma environ-
 226 ments and spacecraft data sets, although the absolute value of each parameter signifi-
 227 cantly varies in different environments. In addition, the solar wind plasma remains calm
 228 and steady for more than five minutes on either side of the structure which reduces the
 229 amount of turbulence and interference at the bow shock and in the magnetosheath and
 230 simplifies the interpretation of time series data.

231

2.2 Arrival at the bow shock

232

233

234

235

236

237

238

239

240

241

242

243

244

245

246

247

248

249

250

251

252

253

At around 09:32:00 UT (corresponding to a ~ 53 minute transition time to the nose of the bow shock from L1), several Earth-orbiting spacecraft are spread across the day-side bow shock, magnetosheath, and magnetopause. Figure 2 shows trajectories of THEMIS, Cluster, and MMS spacecraft projected on the xy (left) and xz (right) planes of the GSM coordinates for a three-hour interval starting at 09:30:00 UT. Before the SWMH arrives at the bow shock, the MMS spacecraft are on an inbound trajectory inside the magnetosheath. THD (THEMIS-D) and THE spacecraft are in the solar wind and near the nose of the bow shock, while THA is inside the magnetosheath and closer to the magnetopause boundary. Cluster1, 2, and 4 spacecraft are inside the magnetosphere boundary layer, with Cluster1 being closest to the boundary at the dusk flank side. In Figure 2, we also show modeled magnetopause (solid lines) and bow shock (dashed lines) boundaries for two sets of upstream conditions. The model parameters including $P_{dyn.}$, the Alfvénic Mach number ($M_{Alf.} = v_{sw}/v_A$, where v_{sw} is the solar wind flow speed along the normal vector at the nose of the bow shock) and the B_z component of the IMF are annotated on the left panel. The grey lines show the standoff distance of boundaries for conditions inside the SWMH (grey parameters). To have a better contrast, the parameters inside the SWMH are selected around the lowest magnetic field strength. The modeled bow shock and magnetopause boundaries in Figure 2 are drawn at the zero plane of the third coordinate. The predicted boundaries are based on statistical models fitted on many bow shock crossings and assume cylindrical symmetry around the aberrated Sun-Earth line. These factors can cause discrepancies between the predicted plasma environment in which each spacecraft resides and in-situ observations.

254

255

256

257

258

259

260

261

Figure 3 shows an overview of in-situ measured plasma and field data from MMS1. The magnetic field data are provided by the magnetometer system (Russell et al., 2016) and plasma particles are probed by the Fast Plasma Investigation (FPI) instrument (Pollock et al., 2016). The spacecraft is initially in the magnetosheath but it emerges out to the solar wind as the RCS hits the bow shock. The magnetic field rotation associated with the onset of the RCS is observed by MMS1 inside the magnetosheath at 09:32:42 UT. The rotation is accompanied by a decrease in the magnetic field strength corresponding to the shocked SWMH plasma. MMS1 remains inside the magnetosheath for another

Table 1. Properties of the SWMH observed by different spacecraft

Region*	source	$\alpha(^{\circ})$	δB	$n^{\dagger}(\text{cm}^{-3})$	$\delta t(\text{s})$	t_i	t_f	β^{\dagger}	$V_{Alf.}^{\dagger}(\text{km/s})$	$r_{GSM}(R_E)$
SW	ACE ⁺	119.6	0.5	5.4(-)	236	8:31:28	8:35:24	5.2(0.48)	32.8(67.4)	(239.7, -15.9, 26.5)
	WIND	118.2	0.69	8.7(6.6)	551	8:39:14	8:48:25	22(1)	22.6(64.9)	(195.7, -29.9, 7.6)
BSh	MMS		0.49	11.5(9.8)	302	9:32:42	9:37:44	20.6(4.2)	23(47.1)	(3.9, 21.1, -2.8)
	THD [‡]	122.3	0.67	-	274	9:33:07	9:37:42	-	-	(11.8, -3.4, 5.9)
	THE [‡]		0.67	-	272	9:33:23	9:37:55	-	-	(11.1, -5.1, 6.3)
MSh	THA	103.2	0.7	37.4(27.5)	335	9:35:27	9:41:03	47.1(2.8)	38.8(125.3)	(9.0, -3.7, 5.8)
MP	C1 ^{††}	-	-	-	30	9:39:16	9:39:46	-	-	(0, 14.5, 2.4)

*SW: Solar wind, BSh: Bow shock, MSh: Magnetosheath, MP: Magnetopause

[†]Values in () are measured outside the magnetic hole

⁺Low time resolution plasma measurements

[‡]Plasma data contaminated by foreshock ions

^{††}Plasma data unavailable, partial encounters

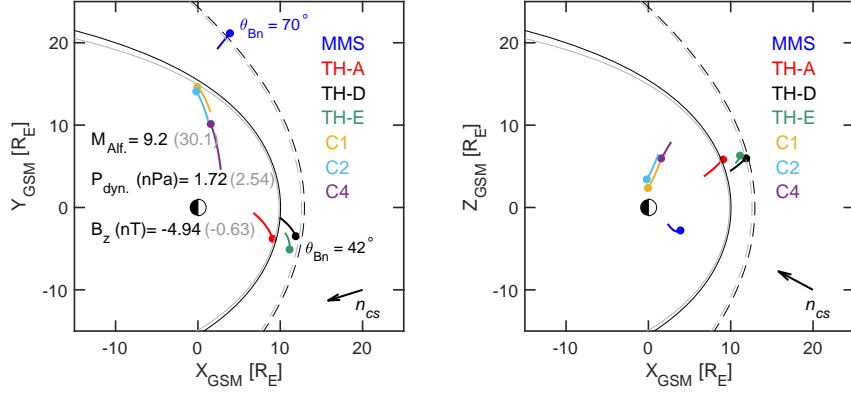


Figure 2. Spacecraft positions projected on the xy (left) and xz (right) planes of GSM coordinates. The MMS1 spacecraft (MMS) is shown in blue, THA in red, THD in black, THE in green, Cluster1 (C1) in yellow, Cluster2 (C2) in cyan, and Cluster4 (C4) in purple. Trajectories are shown for a 3-hour interval between 09:30:00 and 12:30:00 UT on 20 November 2018. Filled circles mark the beginning of the interval. The dashed parabolas represent the bow shock boundary modeled after Farris and Russell (1994), while the solid parabolas are the modeled magnetopause boundary (Shue et al., 1998). The grey boundaries are model predictions under upstream conditions inside the magnetic depression of the RCS. The model parameters are annotated on the left panel. The normal vector to the RCS plane (n_{cs}) is marked on the lower right corner of each panel. The shock angles (θ_{Bn}) correspond to the IMF orientation before the event onset at MMS1 and THD.

119 s before the bow shock layer moves inward past the spacecraft position. At the leading edge of the RCS, the magnetic field clock angle changes from 275° to $\sim 160^\circ$ and in general, both cone and clock angles show similar patterns to those observed in the solar wind, although magnetic field fluctuations are significantly higher in the magnetosheath.

The electron energy spectrogram in Figure 3c shows that the energy flux of accelerated solar wind electrons increases when the SWMH crosses the bow shock, as compared to the distributions in the magnetosheath plasma and before the event onset. As the bow shock recedes, MMS1 crosses a shock layer formed against the SWMH. Inside the SWMH, the shock obliquity decreases but it remains in the quasi-perpendicular regime ($\theta_{Bn} \sim 56^\circ$). The low magnetic energy density and increased plasma density within the hole result in a high plasma β (the ratio of the plasma thermal pressure to magnetic pressure) and low v_A upstream of the shock (see Table 1). Precursor whistler waves are suppressed upstream of the shock (Fairfield, 1974). Instead, we observe high amplitude quasi-periodic magnetic pulsations with a period of 2 s in the spacecraft frame. These waves can play a role in enhancing the population of accelerated electrons. The bulk plasma velocity components in Figure 3d indicate that the solar wind slowdown along the x -axis and deflection along the y -axis are dominant downstream of the bow shock and the reconnection exhausts are obscured in the sheath plasma. There are however, slight differences in the flow velocity in the magnetosheath between the onset of the field rotation and the bow shock crossing at 09:34:38 UT (the dotted line in Figure 3a). For instance, V_y decreases by ~ 17 km/s from 160 to 143 km/s. Similar variations also exist in V_z . These small changes are superimposed on the flow deflection and slowdown incurred at the bow shock, though they are comparable in strength to changes due to reconnection exhausts within the RCS (Figures 1c–e).

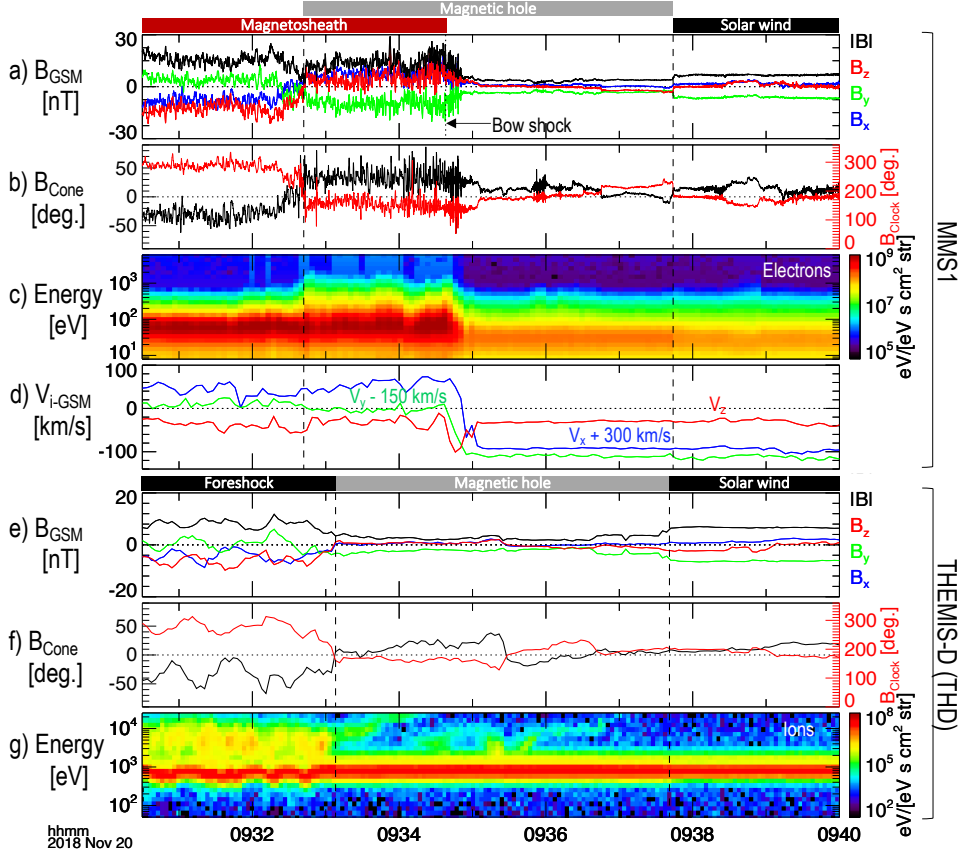


Figure 3. MMS1 and THD observations of the RCS and the SWMH crossing the bow shock. The MMS1 spacecraft is initially in the magnetosheath near the dusk side flank region. Panels (a–d) show MMS1 measurements of the magnetic field components and magnitude, magnetic field cone and clock angles, electron energy spectrogram, and components of the ion bulk flow velocity, respectively. The V_x and V_y velocity components in panel (d) are shifted by +300 km/s and -150 km/s, respectively. Panels (e) and (f) show the magnetic field, and cone and clock angle data from THD spacecraft positioned closer the nose of the bow shock. The vertical dashed lines mark the boundaries of the SWMH as observed by MMS1 and THD. The vertical dotted line on panel (a) marks the bow shock crossing at 09:34:38 UT.

THD observations of the RCS and SWMH are shown in Figures 3e–g. During this time, THD is in the foreshock region upstream of the quasi-parallel side of the shock. THD magnetic field data are from the flux gate magnetometers (Auster et al., 2008), and plasma data are from the electrostatic analyzers (McFadden et al., 2008), and the solid state telescopes. Before the field rotation, THD measures high levels of turbulence (Figure 3e) associated with a significant flux of suprathermal foreshock ions in this region. These ions, visible in the ion energy spectrogram in Figure 3g at energies above the solar wind beam energy at ~ 900 eV, can create plasma waves through a variety of instabilities (Scholer & Burgess, 1992). Rotation of the field at $\sim 09:33:08$ UT results in a traveling foreshock (Kajdić et al., 2017), and disappearance of waves. The shock angle inside the SWMH and immediately after the field rotation is about 72° and it mostly remains above 45° throughout the SWMH passage. The clock angle changes from $\sim 280^\circ$ to 168° , while the cone angle changes from -32° to $\sim 12^\circ$. The THE spacecraft is about $0.7 R_E$ downstream from THD and very close to the bow shock but still in the foreshock

300 region. THE observations (not shown) show similar RCS features to those in THD data,
 301 except that foreshock turbulence at THE is much more intense with sporadic high am-
 302 plitude steepened waves. The density of backstreaming ions is also higher at THE. The
 303 RCS is observed by THE 16 s after THD (as indicated by t_i times in Table 1) correspond-
 304 ing to an average radial solar wind flow speed of 292.8 km/s. This solar wind slowdown
 305 is due to foreshock effects that begin much farther upstream of the shock and beyond
 306 the THD position, as backstreaming ions can travel long distances upstream of the shock
 307 along the magnetic field lines (Eastwood et al., 2005).

308 2.3 Changes in the magnetosheath and at the magnetopause

309 SWMHs can bypass the bow shock and travel through the magnetosheath in the
 310 form of diamagnetic plasmoids (Karlsson et al., 2015). In Figure 3 we showed that the
 311 characteristic field rotation across the RCS in the solar wind can be clearly identified in
 312 magnetosheath plasma immediately downstream of the quasi-perpendicular bow shock
 313 in MMS1 data. During this event, THA is at (9.0, -3.7, 5.8) R_E in the magnetosheath
 314 and downstream of the quasi-parallel side of the bow shock (see the shock angle map in
 315 Figure S2 in the Supplementary Information section). Figure 4a shows magnetic field
 316 cone and clock angles measured by THA, while the magnetic field components and strength
 317 are shown in Figure 4b. Before the structure arrives at THA, the B_x component of the
 318 magnetic field in the sheath plasma is pointing sunward, resulting in a positive cone an-
 319 gle of 14.5° . This B_x reversal at THA is due to draping of the sheath plasma (Coleman,
 320 2005; Spreiter et al., 1966). The clock angle at the leading edge of the structure changes
 321 from 264° to 166° similar to changes observed at THD and MMS1. Foreshock effects cause
 322 noticeable slowdown of the solar wind on the leading edge of the MH compared to the
 323 trailing edge, and the structures trailing edge is processed faster through the shock than
 324 its leading edge. δB at THA is about 0.70, although at times the magnetic field strength
 325 reduces to half of the pristine IMF strength. The level of plasma turbulence inside the
 326 magnetic hole also decreases significantly compared to the surrounding magnetosheath
 327 plasma. Several sporadic magnetic peaks are observed inside the MH that are linearly
 328 polarized and are accompanied by earthward directed transverse electron jets. Ions do
 329 not seem to be affected, which indicates that peaks are on electron kinetic scales. The
 330 magnetic peaks also seem to be unrelated to mirror mode waves as they lack any elec-
 331 tron density enhancements. These peaks tend to propagate in the background ion plasma
 332 rest frame, though their generation mechanism remains unexplained (Yao et al., 2017).

333 In Figure 4e we show the plasma pressure terms including the ion (electron) ther-
 334 mal pressure $P_{i(e)} = n_{i(e)} k_b T_{i(e)}$, where $n_{i(e)}$ and $T_{i(e)}$ are the density and average tem-
 335 perature of ions (electrons), and k_b is the Boltzmann constant. The magnetic pressure
 336 $P_B = |B|^2/2\mu_0$ and the total pressure $P_{tot.} = P_i + P_e + P_B$ are also shown. The de-
 337 crease in the magnetic pressure is compensated by the increase in ion thermal pressure,
 338 so the structure remains roughly pressure balanced as it travels through the magnetosheath.
 339 The flow dynamic pressure $P_{dyn.}$ is also shown on this panel to emphasize that although
 340 there are no high-speed (ion) plasma jets, the dynamic pressure within the MH is sig-
 341 nificantly higher than the surrounding magnetosheath plasma, and at times even higher
 342 than half the solar wind dynamic pressure (horizontal dotted line), which is a thresh-
 343 old used in some studies to identify magnetosheath jets (Escoubet et al., 2020). Vari-
 344 ations in $P_{dyn.}$ are driven by n_i which is affected by the propagation pattern of the RCS
 345 in the magnetosheath.

346 Figures 4f and g show electron and ion energy spectra measured at three timestamps
 347 before, within, and after the MH. Inside the MH, electron and ion energy distributions
 348 broadens, with a higher flux of accelerated particles in the few keV range. Accelerated
 349 electrons remain restricted to the MH boundaries showing more abundance near the cen-
 350 ter. They are likely remnants of heating and acceleration processes at the bow shock rather
 351 than being generated at a nearby magnetopause reconnection zone. Although THA is

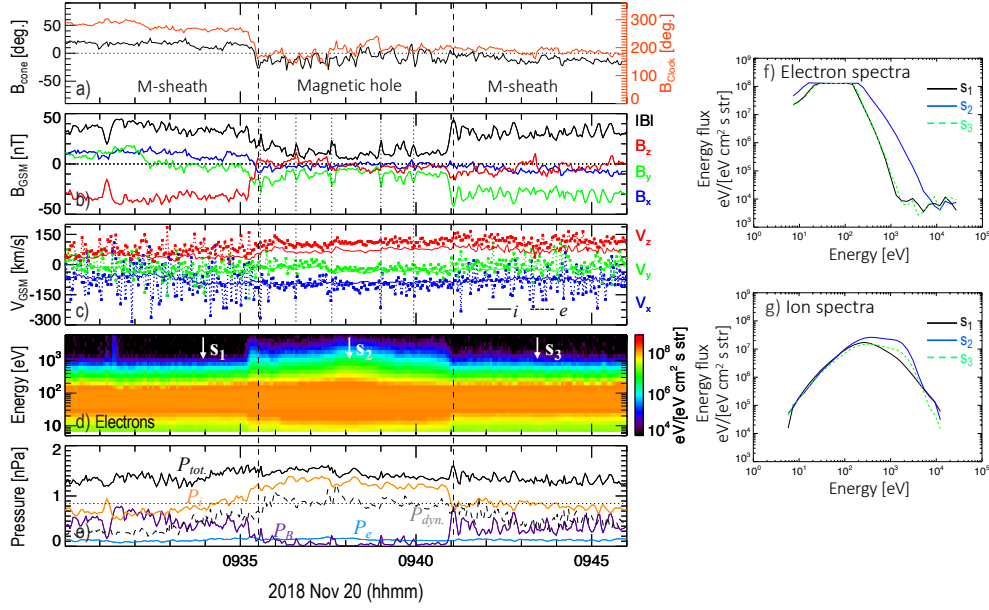


Figure 4. Observations of the RCS in the magnetosheath by THA. Panels show: (a) the cone and clock angles, and annotated magnetosheath (M-sheath) and magnetic hole intervals, (b) magnetic field components and strength, (c) ion (solid lines) and electron (dotted lines) velocity components, (d) electron energy spectrogram, (e) pressure terms including the electron thermal pressure (P_e , blue), ion thermal pressure (P_i , red), magnetic pressure (P_B , purple), dynamic pressure ($P_{dyn.}$, grey-dotted), and the total pressure ($P_{tot.}$, black). The horizontal dashed line in panel (e) is drawn at half the pristine solar wind dynamic pressure (0.86 nPa). The two vertical dashed lines on these panels mark the magnetic hole boundaries, while vertical dotted lines in panels (b–c) correspond to a select number of magnetic peaks inside the hole to emphasize their association with electron jets. Panels (f) and (g) show, respectively, electron and ion energy spectra at three timestamps identified on panel (d).

close to the magnetopause boundary, there are no ion jets in the data to indicate proximity to a reconnection zone. The electron temperature inside the magnetic hole is isotropic, and the average electron temperature slightly reduces from the ambient magnetosheath plasma. The ion temperature is anisotropic, with higher temperatures perpendicular to the field. The density and the average temperature of ions increase inside the MH. Changes in particle energy distributions have implications for energy input at the magnetopause which we discuss in Section 3.3.

Variations in the plasma dynamic pressure can have an influence on the shape of the magnetopause and its standoff distance. The upstream IMF variations can also dramatically change the magnetic field topology and reconnection zones at the magnetopause (Trattner et al., 2016, 2020). We use a model to estimate the probable magnetic field topology at the magnetopause and calculate the maximum magnetic shear angle between the convected IMF and the geomagnetic field (Trattner et al., 2007). The model takes into account convection of the solar wind through the magnetosheath, geomagnetic field at the magnetopause, and draping effects, to predict regions across the magnetopause prone to reconnection. In Figure 5a we show the maximum shear angle map at the magnetopause for solar wind conditions before the onset of the RCS when the IMF is southward. High magnetic shear angles (red colors) are formed along the y -axis and mostly above the magnetic equatorial plane. The white streaks are regions with almost exactly

371 anti-parallel field configuration. The map in Figure 5b is generated based on plasma condi-
 372 tions within the SWMH, where the dynamic pressure has increased and B_z is very small.
 373 The white line connecting the two loci is the predicted component reconnection line that
 374 extends more than $15 R_E$ across the magnetopause. Under SWMH plasma conditions,
 375 model predictions suggest that Cluster1 and 2 spacecraft are farther from active recon-
 376 nection zones and are outside the magnetopause boundary.

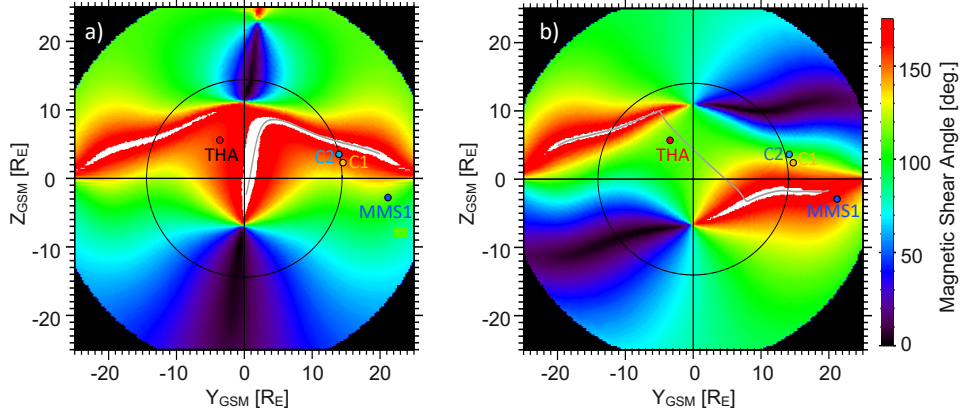


Figure 5. Maps of the magnetic shear angle between the convected IMF and the dipole field, and possible reconnection zones at the magnetopause. Each map shows a cross-sectional view of the magnetopause (black circle) viewed from the Sun. (a) The shear angle map at the magnetopause under convected solar wind conditions before the RCS onset (i.e., $-B_z$), (b) shear angles based on the solar wind conditions inside the magnetic hole. The white streaks are regions with almost exactly anti-parallel field configuration (within 3°). The positions of THA, MMS1, Cluster1, Cluster2 spacecraft are identified for reference.

377 Indeed all Cluster spacecraft are initially inside the boundary layer, consistent with
 378 model predictions. Cluster1 and 2 are near the flank region of the magnetopause on the
 379 dusk side and downstream of the quasi-perpendicular side of the bow shock, while Clus-
 380 ter4 is deeper inside the magnetosphere and farther away from the magnetopause bound-
 381 ary. Magnetic field measurements from Cluster1, 2, and 4 (Balogh et al., 2001) are shown
 382 in Figure 6. All three spacecraft observe perturbations in the geomagnetic field between
 383 09:36:30 and 09:41:30 UT, corresponding to the time when the solar wind RCS entered
 384 the magnetosheath. Magnetic perturbations decrease with spacecraft distance to the mag-
 385 netopause. Cluster1 is closest to the magnetopause boundary and records the highest
 386 level of magnetic fluctuations that include B_z field reversals. The only source of $-B_z$ at
 387 the position of Cluster1 inside the boundary layer is from the magnetosheath plasma and
 388 specifically from the period before the onset of the RCS. After crossing the bow shock
 389 and travelling through the magnetosheath, the RCS impacts the magnetopause and causes
 390 an inward motion of the boundary near Cluster1. The gradual boundary crossing on one
 391 side is followed by a fast rebound on the other side as evident in B_z variations. The Clus-
 392 ter2 spacecraft is $\sim 0.4 R_E$ apart from Cluster1 along the local normal direction to the
 393 magnetopause, but it does not see the motion of the boundary.

394 3 Discussion

395 Based on correlated and anti-correlated variations in B_y and V_y , enhancements in
 396 plasma density and temperature, and the high magnetic shear angle we classify the mag-
 397 netic depression event between 08:39:14 and 08:48:25 UT in Wind data as an RCS. We

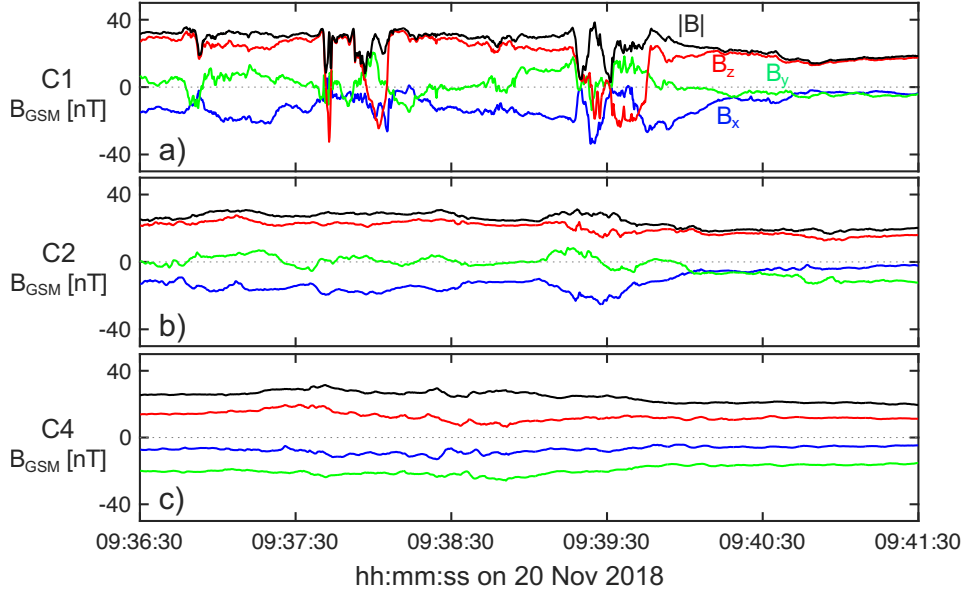


Figure 6. Three Cluster spacecraft observations of the event inside the magnetosphere boundary layer. Panels (a – c) show the magnetic field data from Cluster 1, 2, and 4, respectively.

398 track the structure in other plasma environments by observing the distinct change in the
 399 magnetic field clock angle, followed by a depression in the magnetic field strength, and
 400 an increase in plasma density. These characteristics are consistently observed in differ-
 401 ent data sets and plasma environments but with varying values and ranges (see Table 1).
 402 We determine the structure’s orientation in the solar wind and show how it impacts the
 403 bow shock and magnetopause using observations from multiple Earth orbiting spacecraft.
 404 The normal vector to the RCS plane at ACE is about 8° different than that at Wind.
 405 The event duration also increases from ACE to Wind, and then decreases at MMS1 near
 406 the bow shock. These differences can be due to the rotation of the RCS plane during the
 407 transit from L1 to Earth’s bow shock. Ongoing reconnection and plasma instabilities can
 408 also modify the current sheet structure.

3.1 Asymmetric interaction and global impact

409
 410 THD and MMS1 spacecraft are separated by more than $27 R_E$ across the bow shock,
 411 while THA and Cluster 1 are $\sim 20 R_E$ apart across the magnetopause boundary. We show
 412 that, with certain time lags, all spacecraft measured signatures of the same structure which
 413 suggests that the solar wind RCS plane covers most of the dayside bow shock surface.
 414 Even though MMS1 is $7.2 R_E$ downstream of THD and in the magnetosheath, it observes
 415 the structure 24 s before THD, indicating that the RCS with high momentum plasma
 416 enters the magnetosheath through the flank region of the bow shock first and then through
 417 the subsolar region. This order of observations also agrees with our estimate of the RCS
 418 plane orientation which hits the $(+x, +y, -z)$ quadrant of the bow shock first. Further-
 419 more, before the SWMH arrival, THD is upstream of the quasi-parallel side of the shock,
 420 where foreshock effects tend to significantly decelerate the solar wind. Backstreaming
 421 foreshock ions travel far distances upstream of the shock along the magnetic field line
 422 and perturb the solar wind. As such, the upstream structure arrives at and crosses the
 423 quasi-perpendicular side of the bow shock before the quasi-parallel side (Turc et al., 2020).
 424 This asymmetric interaction across the bow shock will inevitably transfer downstream
 425 and create asymmetric interaction zones at the magnetopause boundary (Keika et al.,
 426 2009; Webster et al., 2021).

427
 428
 429
 430
 431
 432
 433
 434
 435
 436
 437
 438
 439
 440
 441

The schematic in Figure 7 shows a summary of our observations, illustrating the dynamics of the RCS interaction at different stages and environments. The schematic shows that parts of the bow shock and magnetopause are displaced and pushed inward after interacting with the RCS. THA and MMS1 observations of magnetosheath plasma indicate that inside the MH, B_z is essentially zero or even slightly positive. However, because of the misalignment of the RCS plane normal vector with the solar wind velocity vector and asymmetric effects discussed earlier, when parts of the magnetopause are pushed inward, Cluster1 observes magnetosheath flow with $-B_z$ field originated from upstream regions near the subsolar point where the RCS has not reached yet (\vec{V}_{MSH} in Figure 7). Since the bow shock and the magnetopause are essentially local pressure-balanced boundaries between two plasma environments, the asymmetric interaction of the RCS results in deformed boundaries. As the schematic in Figure 7 shows, the bow shock (and the magnetopause) adjusts itself in response to a change in the direction of the highest dynamic pressure, which in this case is caused by the increase in plasma density within the RCS and its propagation direction is aligned with the RCS plane orientation.

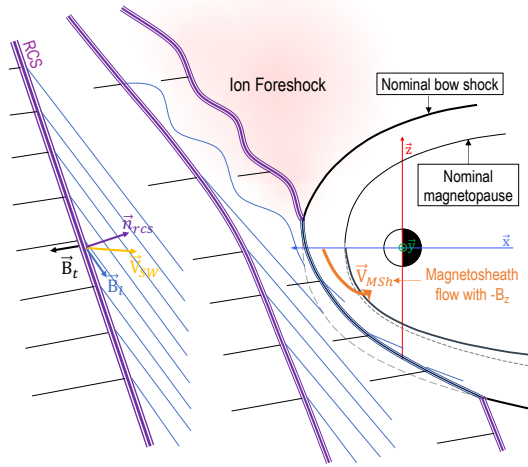


Figure 7. A schematic illustration of the RCS and the SWMH (purple line) interacting with the bow shock and the magnetopause. The magnetic field lines on the leading edge (\vec{B}_l) are indicated with blue lines. The magnetic field lines on the trailing edge (\vec{B}_t) are shown in black. The solar wind flow vector (\vec{V}_{SW}) and the normal vector the RCS plane (\vec{n}_{RCS}) are also shown. The magnetosheath plasma flow carrying $-B_z$ field downstream of the bow shock is indicated with \vec{V}_{MSH} . The dashed line segments indicate the nominal position of the boundaries before the start of the interaction with the RCS.

 442
 443
 444
 445
 446
 447
 448
 449

3.2 Energy input and reconnection at the magnetopause

Ion and electron velocities in Figure 4c show that THA observes a draped plasma flow pointed mostly Earth-ward and northward, which is consistent with the position of THA in the magnetosheath. At the leading edge of the magnetic hole, field rotation is accompanied by an increase in V_z , suggesting that flow deflection increases as the structure propagates through the magnetosheath. This flow pattern is consistent with the asymmetric encounter of the solar wind RCS plane with the bow shock, which can preferentially drive the magnetosheath plasma along its normal vector.

 450
 451
 452

The electron and ion energy spectra lines in Figures 4f–g show clear enhancements in the flux of accelerated electrons and ions inside the MH. Once these particles reach the magnetopause, they can travel along the geomagnetic field lines and precipitate into

453 the ionosphere through cusp regions. Accelerated electrons are also present in Figure 3c
 454 in the portion of the MH that has crossed the bow shock, indicating that acceleration
 455 of electrons to high energies is associated with RCS and SWMH interactions at the bow
 456 shock. Low v_A and high plasma β within the SWMH and upstream of the bow shock
 457 also have implications for generation of upstream instabilities (Gary, 1993; Madanian
 458 et al., 2021; Petrukovich & Chugunova, 2021). When magnetosheath is dominated by
 459 the MH plasma, coupling of the solar wind to the magnetosphere shifts to the low-latitude
 460 boundary layer (closed field lines), and through hydrodynamic forcing (Maynard et al.,
 461 2011). Large-scale RCS and SWMH events change the rate of energy input into the ionosphere-
 462 magnetosphere system either by introducing precipitating accelerated particles or by mod-
 463 ulating the ion transport at ionospheric altitudes near the polar cap regions. More ob-
 464 servational and simulation studies are required in the future to characterize their effects
 465 in those plasma environments. We should also note that THA moment data in Figure 4
 466 are calculated onboard the spacecraft with measurements performed in the reduced mode
 467 (i.e., reduced energy and spatial resolutions). The high time resolution of data in this
 468 mode however, enables studying physical processes on time scales relevant to the RCS
 469 duration. There may be minor calibration issues in data, for instance the difference be-
 470 tween the electron and ion V_z velocity component, or electron flux saturation at high
 471 count rates which relates to the instrument sensitivity in this mode. Our results and in-
 472 terpretations are not affected by these issues.

473 Crossing the bow shock can also modify the exhaust flows within the RCS, which
 474 can disrupt any ongoing reconnection process (Phan et al., 2011). Survival of the recon-
 475 nection jets across the bow shock is dependent upon the direction of reconnection ex-
 476 hausts and the bow shock geometry at the point of crossing, which can further contribute
 477 to creating variable plasma environments downstream of the bow shock. When the so-
 478 lar wind IMF has already been depleted, for instance through reconnection within the
 479 solar wind, the dynamics of reconnection at the magnetopause can become more com-
 480 plicated. Rotation of the magnetic field across the event studied in this paper reduces
 481 regions of high magnetic shear angles across the magnetopause (Figure 5b). In addition,
 482 the plasma β inside the MH is higher than the surrounding magnetosheath plasma, and
 483 much higher than the low-density plasma in the boundary layer. These conditions seem
 484 to have adverse effects on the reconnection rate at the magnetopause.

485 4 Conclusion

486 In this study, we follow an RCS initially observed in the pristine solar wind upstream
 487 of Earth across the bow shock, and through the magnetosheath to the magnetopause.
 488 Reconnection in the solar wind converts the IMF energy into plasma kinetic energy, thus
 489 depleting the magnetic field strength within the current sheet, while increasing the plasma
 490 density and temperature and creating a high momentum plasma layer. Rotational SWMHs
 491 associated with RCS are caused by magnetic reconnection and show noticeable enhance-
 492 ment in both plasma density and temperature. Once reconnection begins in the solar
 493 wind flow, there is abundant magnetic energy in the IMF available to the process, and
 494 therefore the amount of density buildup and the spatial scale of the magnetic depres-
 495 sion can be significant. We show that the RCS enters the bow shock through the flank
 496 regions rather than the subsolar point. Upon crossing the bow shock, acceleration of so-
 497 lar wind electrons is more efficient within the magnetically depleted layer, and accel-
 498 erated electrons remain restricted to the MH inside the magnetosheath (Figure 4d). De-
 499 termining the nature of the acceleration mechanism at the bow shock and its relation
 500 to high amplitude waves are left for our future studies.

501 The RCS and its SWMH form a high dynamic pressure plasma layer inside the mag-
 502 netosheath. Given the global nature of the interaction, it would be a misnomer to cat-
 503 egorize such a structure as a plasma jet, although it may very well fit the selection cri-
 504 teria of high speed jets (i.e., enhanced dynamic pressure above half the solar dynamic

505 pressure). Nonetheless, similar to high-speed jets, RCS and their SWMHs can cause asym-
 506 metric deformation of the magnetopause boundary, and modulate the reconnection rate.
 507 Furthermore, the amplitude of magnetic perturbations due to the RCS decreases with
 508 distance from the magnetosphere boundary layer (Figure 6), and Earth's magnetosphere
 509 seems to act as a "cushion" against the upstream high momentum plasma anomaly. Ef-
 510 fects of the RCS and SWMH structures on planets without an intrinsic magnetosphere
 511 merit further investigations in the future.

512 Acknowledgments

513 We thank the mission operation and instrument teams on ACE, Wind, THEMIS, Clus-
 514 ter, and MMS missions for making their science data available. All data used in this study
 515 are publicly accessible through <https://spdf.gsfc.nasa.gov/pub/data/>. This work
 516 was partially supported by National Aeronautics and Space Administration (NASA) grants
 517 NNG04EB99C and 80NSSC21K1461. KJT efforts were supported in part by NASA grant
 518 80NSSC20K0688. HM thanks support from an ISSI team on magnetic holes.

519 References

- 520 Andreeova, K., Pulkkinen, T. I., Palmroth, M., & McPherron, R. (2011). Geo-
 521 efficiency of solar wind discontinuities. *Journal of Atmospheric and Solar-*
 522 *Terrestrial Physics*, *73*(1), 112–122. doi: 10.1016/j.jastp.2010.03.006
- 523 Angelopoulos, V. (2008). The THEMIS mission. *Space Science Reviews*, *141*(1-4),
 524 5–34. doi: 10.1007/s11214-008-9336-1
- 525 Archer, M. O., Horbury, T. S., & Eastwood, J. P. (2012, 5). Magnetosheath pres-
 526 sure pulses: Generation downstream of the bow shock from solar wind dis-
 527 continuities. *Journal of Geophysical Research: Space Physics*, *117*(5). doi:
 528 10.1029/2011JA017468
- 529 Auster, H. U., Glassmeier, K. H., Magnes, W., Aydogar, O., Baumjohann, W.,
 530 Constantinescu, D., ... Wiedemann, M. (2008). The THEMIS flux-
 531 gate magnetometer. *Space Science Reviews*, *141*(1-4), 235–264. doi:
 532 10.1007/s11214-008-9365-9
- 533 Balikhin, M. A., Sibeck, D. G., Runov, A., & Walker, S. N. (2012, 8). Mag-
 534 netic holes in the vicinity of dipolarization fronts: Mirror or tearing struc-
 535 tures? *Journal of Geophysical Research: Space Physics*, *117*(8). doi:
 536 10.1029/2012JA017552
- 537 Balogh, A., Carr, C. M., Acuña, M. H., Dunlop, M. W., Beek, T. J., Brown, P., ...
 538 Schwingenschuh, K. (2001, 9). The Cluster Magnetic Field Investigation:
 539 overview of in-flight performance and initial results. *Annales Geophysicae*,
 540 *19*(10/12), 1207–1217. doi: 10.5194/angeo-19-1207-2001
- 541 Blanco-Cano, X., Preisser, L., Kajdič, P., & Rojas-Castillo, D. (2020). Magne-
 542 tosheath Microstructure: Mirror Mode Waves and Jets during Southward IP
 543 Magnetic Field. *Journal of Geophysical Research: Space Physics*, *125*(9). doi:
 544 10.1029/2020JA027940
- 545 Burch, J. L., Moore, T. E., Torbert, R. B., & Giles, B. L. (2016, 3). Magnetospheric
 546 Multiscale Overview and Science Objectives. *Space Science Reviews*, *199*(1-4),
 547 5–21. doi: 10.1007/s11214-015-0164-9
- 548 Burlaga, L. F., Ness, N. F., & Acuna, M. H. (2007, 7). Linear magnetic holes in a
 549 unipolar region of the heliosheath observed by Voyager. *Journal of Geophysical*
 550 *Research: Space Physics*, *112*(7). doi: 10.1029/2007JA012292
- 551 Burlaga, L. F., Scudder, J. D., Klein, L. W., & Isenberg, P. A. (1990). Pressure-
 552 Balanced structures between 1 AU and 24 AU and their implications for solar
 553 wind electrons and interstellar pickup ions. *Journal of Geophysical Research*,
 554 *95*(A3), 2229. doi: 10.1029/ja095ia03p02229
- 555 Cassak, P. A., & Shay, M. A. (2007). Scaling of asymmetric magnetic reconnect-

- 556 tion: General theory and collisional simulations. *Physics of Plasmas*, 14(10),
557 102114. doi: 10.1063/1.2795630
- 558 Coleman, I. J. (2005). A multi-spacecraft survey of magnetic field line draping in the
559 dayside magnetosheath. *Annales Geophysicae*, 23(3), 885–900. doi: 10.5194/
560 angeo-23-885-2005
- 561 Drake, J. F., Swisdak, M., Opher, M., & Richardson, J. D. (2017). The For-
562 mation of Magnetic Depletions and Flux Annihilation Due to Reconnec-
563 tion in the Heliosheath. *The Astrophysical Journal*, 837(2), 159. doi:
564 10.3847/1538-4357/aa6304
- 565 Eastwood, J. P., Lucek, E. A., Mazelle, C., Meziane, K., Narita, Y., Pickett, J., &
566 Treumann, R. A. (2005, 6). The foreshock. *Space Science Reviews*, 118(1-4),
567 41–94. doi: 10.1007/s11214-005-3824-3
- 568 Escoubet, C. P., Fehringer, M., & Goldstein, M. (2001, 9). The Cluster mission. *An-
569 nales Geophysicae*, 19(10/12), 1197–1200. doi: 10.5194/angeo-19-1197-2001
- 570 Escoubet, C. P., Hwang, K. J., Toledo-Redondo, S., Turc, L., Haaland, S. E.,
571 Aunai, N., ... Torbert, R. B. (2020). Cluster and MMS Simultaneous
572 Observations of Magnetosheath High Speed Jets and Their Impact on the
573 Magnetopause. *Frontiers in Astronomy and Space Sciences*, 6, 78. doi:
574 10.3389/fspas.2019.00078
- 575 Fairfield, D. H. (1974, 4). Whistler waves observed upstream from collision-
576 less shocks. *Journal of Geophysical Research*, 79(10), 1368–1378. doi:
577 10.1029/ja079i010p01368
- 578 Farris, M. H., & Russell, C. T. (1994). Determining the standoff distance of the
579 bow shock: Mach number dependence and use of models. *Journal of Geophysi-
580 cal Research*, 99(A9), 17681. doi: 10.1029/94ja01020
- 581 Farrugia, C. J., Erkaev, N. V., Biernat, H. K., & Burlaga, L. F. (1995). Anoma-
582 lous magnetosheath properties during Earth passage of an interplanetary
583 magnetic cloud. *Journal of Geophysical Research*, 100(A10), 19245. doi:
584 10.1029/95ja01080
- 585 Gary, S. P. (1993). *Theory of Space Plasma Microinstabilities*. Cambridge: Cam-
586 bridge University Press. doi: 10.1017/cbo9780511551512
- 587 Gosling, J. T. (2012). Magnetic reconnection in the solar wind. *Space Science Re-
588 views*, 172(1-4), 187–200. doi: 10.1007/s11214-011-9747-2
- 589 Gosling, J. T., Skoug, R. M., McComas, D. J., & Smith, C. W. (2005). Di-
590 rect evidence for magnetic reconnection in the solar wind near 1 AU.
591 *Journal of Geophysical Research: Space Physics*, 110(A1), A01107. doi:
592 10.1029/2004JA010809
- 593 Gosling, J. T., & Szabo, A. (2008). Bifurcated current sheets produced by mag-
594 netic reconnection in the solar wind. *Journal of Geophysical Research: Space
595 Physics*, 113(10). doi: 10.1029/2008JA013473
- 596 Hamrin, M., Gunell, H., Goncharov, O., DeSpiegeleer, A., Fuselier, S., Mukherjee,
597 J., ... Giles, B. (2019). Can Reconnection be Triggered as a Solar Wind Di-
598 rectional Discontinuity Crosses the Bow Shock? A Case of Asymmetric Recon-
599 nection. *Journal of Geophysical Research: Space Physics*, 124(11), 8507–8523.
600 doi: 10.1029/2019JA027006
- 601 Harten, R., & Clark, K. (1995, 2). The design features of the GGS wind and polar
602 spacecraft. *Space Science Reviews*, 71(1-4), 23–40. doi: 10.1007/BF00751324
- 603 Hesse, M., & Cassak, P. A. (2020). Magnetic Reconnection in the Space Sciences:
604 Past, Present, and Future. *Journal of Geophysical Research: Space Physics*,
605 125(2). doi: 10.1029/2018ja025935
- 606 Hietala, H., Phan, T. D., Angelopoulos, V., Oieroset, M., Archer, M. O., Karls-
607 son, T., & Plaschke, F. (2018). In Situ Observations of a Magnetosheath
608 High-Speed Jet Triggering Magnetopause Reconnection. *Geophysical Research
609 Letters*, 45(4), 1732–1740. doi: 10.1002/2017GL076525
- 610 Hietala, H., & Plaschke, F. (2013). On the generation of magnetosheath high-speed

- 611 jets by bow shock ripples. *Journal of Geophysical Research: Space Physics*,
612 *118*(11), 7237–7245. doi: 10.1002/2013JA019172
- 613 Kahler, S., Crooker, N. U., & Gosling, J. T. (1998, 9). Properties of interplanetary
614 magnetic sector boundaries based on electron heat-flux flow directions. *Journal*
615 *of Geophysical Research: Space Physics*, *103*(A9), 20603–20612. doi: 10.1029/
616 98JA01745
- 617 Kahler, S., & Lin, R. P. (1994). The determination of interplanetary magnetic field
618 polarities around sector boundaries using E \geq 2 keV electrons. *Geophysical Re-*
619 *search Letters*, *21*(15), 1575–1578. doi: 10.1029/94GL01362
- 620 Kajdić, P., Blanco-Cano, X., Omid, N., Rojas-Castillo, D., Sibeck, D. G., & Billing-
621 ham, L. (2017, 9). Traveling Foreshocks and Transient Foreshock Phenomena.
622 *Journal of Geophysical Research: Space Physics*, *122*(9), 9148–9168. doi:
623 10.1002/2017JA023901
- 624 Karlsson, T., Heyner, D., Volwerk, M., Morooka, M., Plaschke, F., Goetz, C., &
625 Hadid, L. (2021). Magnetic Holes in the Solar Wind and Magnetosheath
626 Near Mercury. *Journal of Geophysical Research: Space Physics*, *126*(5). doi:
627 10.1029/2020JA028961
- 628 Karlsson, T., Kullen, A., Liljeblad, E., Brenning, N., Nilsson, H., Gunell, H., &
629 Hamrin, M. (2015, 9). On the origin of magnetosheath plasmoids and their
630 relation to magnetosheath jets. *Journal of Geophysical Research A: Space*
631 *Physics*, *120*(9), 7390–7403. doi: 10.1002/2015JA021487
- 632 Karlsson, T., Liljeblad, E., Kullen, A., Raines, J. M., Slavin, J. A., & Sundberg, T.
633 (2016, 9). Isolated magnetic field structures in Mercury’s magnetosheath as
634 possible analogues for terrestrial magnetosheath plasmoids and jets. *Planetary*
635 *and Space Science*, *129*, 61–73. doi: 10.1016/j.pss.2016.06.002
- 636 Keika, K., Nakamura, R., Baumjohann, W., Angelopoulos, V., Kabin, K., Glass-
637 meier, K. H., ... Rankin, R. (2009). Deformation and evolution of solar wind
638 discontinuities through their interactions with the Earth’s bow shock. *Journal*
639 *of Geophysical Research: Space Physics*, *114*(9). doi: 10.1029/2008JA013481
- 640 Khotyaintsev, Y. V., Graham, D. B., Norgren, C., & Vaivads, A. (2019). Collision-
641 less Magnetic Reconnection and Waves: Progress Review. *Frontiers in Astron-*
642 *omy and Space Sciences*, *6*, 70. doi: 10.3389/fspas.2019.00070
- 643 Kropotina, J. A., Webster, L., Artemyev, A. V., Bykov, A. M., Vainchtein, D. L.,
644 & Vasko, I. Y. (2021). Solar Wind Discontinuity Transformation at the Bow
645 Shock. *The Astrophysical Journal*, *913*(2), 142. doi: 10.3847/1538-4357/
646 abf6c7
- 647 Liemohn, M. W., & Welling, D. T. (2016, 10). Ionospheric and Solar Wind Con-
648 tributions to Magnetospheric Ion Density and Temperature throughout the
649 Magnetotail. In C. R. Chappell, R. W. Schunk, P. M. Banks, J. L. Burch, &
650 R. M. Thorne (Eds.), *Geophysical monograph series* (pp. 101–114). Hoboken,
651 NJ, USA: John Wiley & Sons, Inc. doi: 10.1002/9781119066880.ch8
- 652 Lin, Y. (1997, 11). Generation of anomalous flows near the bow shock by its in-
653 teraction with interplanetary discontinuities. *Journal of Geophysical Research:*
654 *Space Physics*, *102*(A11), 24265–24281. doi: 10.1029/97JA01989
- 655 Madanian, H., Desai, M. I., Schwartz, S. J., Wilson, L. B., Fuselier, S. A., Burch,
656 J. L., ... Lindqvist, P.-A. (2021, 2). The Dynamics of a High Mach Number
657 Quasi-perpendicular Shock: MMS Observations. *The Astrophysical Journal*,
658 *908*(1), 40. doi: 10.3847/1538-4357/abcb88
- 659 Madanian, H., Halekas, J. S., Mazelle, C. X., Omid, N., Espley, J. R., Mitchell,
660 D. L., & McFadden, J. P. (2020, 12). Magnetic Holes Upstream of the Martian
661 Bow Shock: MAVEN Observations. *Journal of Geophysical Research: Space*
662 *Physics*, *125*(1). doi: 10.1029/2019JA027198
- 663 Maynard, N. C., Farrugia, C. J., Burke, W. J., Ober, D. M., Scudder, J. D., Mozer,
664 F. S., ... Siebert, K. D. (2011). Interactions of the heliospheric current and
665 plasma sheets with the bow shock: Cluster and Polar observations in the mag-

- 666 netosheath. *Journal of Geophysical Research: Space Physics*, 116(1), n/a–n/a.
667 doi: 10.1029/2010JA015872
- 668 Maynard, N. C., Farrugia, C. J., Ober, D. M., Burke, W. J., Dunlop, M., Mozer,
669 F. S., ... Siebert, K. D. (2008). Cluster observations of fast shocks in the
670 magnetosheath launched as a tangential discontinuity with a pressure increase
671 crossed the bow shock. *Journal of Geophysical Research: Space Physics*,
672 113(10). doi: 10.1029/2008JA013121
- 673 McFadden, J. P., Carlson, C. W., Larson, D., Ludlam, M., Abiad, R., Elliott,
674 B., ... Angelopoulos, V. (2008). The THEMIS ESA plasma instrument
675 and in-flight calibration. *Space Science Reviews*, 141(1-4), 277–302. doi:
676 10.1007/s11214-008-9440-2
- 677 Mistry, R., Eastwood, J. P., Phan, T. D., & Hietala, H. (2015, 12). Development of
678 bifurcated current sheets in solar wind reconnection exhausts. *Geophysical Re-*
679 *search Letters*, 42(24). doi: 10.1002/2015GL066820
- 680 Osman, K. T., Matthaeus, W. H., Gosling, J. T., Greco, A., Servidio, S., Hnat,
681 B., ... Phan, T. D. (2014). Magnetic reconnection and intermittent tur-
682 bulence in the solar wind. *Physical Review Letters*, 112(21), 215002. doi:
683 10.1103/PhysRevLett.112.215002
- 684 Parker, E. N. (1957). Sweet's mechanism for merging magnetic fields in conduct-
685 ing fluids. *Journal of Geophysical Research*, 62(4), 509–520. doi: 10.1029/
686 jz062i004p00509
- 687 Paschmann, G., Haerendel, G., Papamastorakis, I., Sckopke, N., Bame, S. J.,
688 Gosling, J. T., & Russell, C. T. (1982). Plasma and magnetic field charac-
689 teristics of magnetic flux transfer events. *Journal of Geophysical Research*,
690 87(A4), 2159. doi: 10.1029/JA087iA04p02159
- 691 Paschmann, G., Øieroset, M., & Phan, T. (2013, 10). In-Situ Observations of Re-
692 connection in Space. *Space Science Reviews*, 178(2-4), 385–417. doi: 10.1007/
693 s11214-012-9957-2
- 694 Petrukovich, A. A., & Chugunova, O. M. (2021). Detailed Structure of Very High-
695 β Earth Bow Shock. *Journal of Geophysical Research: Space Physics*, 126(8).
696 doi: 10.1029/2020JA029004
- 697 Petschek, H. E. (1964). Magnetic Field Annihilation. *The Physics of Solar Flares*,
698 *Proceedings of the AAS-NASA Symposium*, 50, 425.
- 699 Phan, T. D., Gosling, J. T., & Davis, M. S. (2009). Prevalence of extended recon-
700 nection X-lines in the solar wind at 1 AU. *Geophysical Research Letters*, 36(9),
701 L09108. doi: 10.1029/2009GL037713
- 702 Phan, T. D., Gosling, J. T., Davis, M. S., Skoug, R. M., Øieroset, M., Lin, R. P.,
703 ... Balogh, A. (2006). A magnetic reconnection X-line extending more
704 than 390 Earth radii in the solar wind. *Nature*, 439(7073), 175–178. doi:
705 10.1038/nature04393
- 706 Phan, T. D., Gosling, J. T., Paschmann, G., Pasma, C., Drake, J. F., Øieroset,
707 M., ... Davis, M. S. (2010). The dependence of magnetic reconnection
708 on plasma β and magnetic shear: Evidence from solar wind observa-
709 tions. *Astrophysical Journal Letters*, 719(2 PART 2), L199–L203. doi:
710 10.1088/2041-8205/719/2/L199
- 711 Phan, T. D., Love, T. E., Gosling, J. T., Paschmann, G., Eastwood, J. P., Øieroset,
712 M., ... Auster, U. (2011). Triggering of magnetic reconnection in a magne-
713 tosheath current sheet due to compression against the magnetopause. *Geophys-*
714 *ical Research Letters*, 38(17). doi: 10.1029/2011GL048586
- 715 Phan, T. D., Paschmann, G., Twitty, C., Mozer, F. S., Gosling, J. T., Eastwood,
716 J. P., ... Lucek, E. A. (2007, 7). Evidence for magnetic reconnection initiated
717 in the magnetosheath. *Geophysical Research Letters*, 34(14), L14104. doi:
718 10.1029/2007GL030343
- 719 Plaschke, F., Hietala, H., & Angelopoulos, V. (2013). Anti-sunward high-speed jets
720 in the subsolar magnetosheath. *Annales Geophysicae*, 31(10), 1877–1889. doi:

- 721 10.5194/angeo-31-1877-2013
- 722 Pollock, C., Moore, T., Jacques, A., Burch, J., Gliese, U., Saito, Y., ... Zeuch, M.
- 723 (2016, 3). Fast Plasma Investigation for Magnetospheric Multiscale. *Space*
- 724 *Science Reviews*, 199(1-4), 331–406. doi: 10.1007/s11214-016-0245-4
- 725 Russell, C. T., Anderson, B. J., Baumjohann, W., Bromund, K. R., Dearborn,
- 726 D., Fischer, D., ... Richter, I. (2016, 3). *The Magnetospheric Multi-*
- 727 *scale Magnetometers* (Vol. 199) (No. 1-4). Springer Netherlands. doi:
- 728 10.1007/s11214-014-0057-3
- 729 Šafránková, J., Němeček, Z., Přech, L., Samsonov, A. A., Koval, A., & Andréevová,
- 730 K. (2007). Modification of interplanetary shocks near the bow shock and
- 731 through the magnetosheath. *Journal of Geophysical Research: Space Physics*,
- 732 112(8), n/a–n/a. doi: 10.1029/2007JA012503
- 733 Scholer, M., & Burgess, D. (1992). The role of upstream waves in supercritical
- 734 quasi-parallel shock re-formation. *Journal of Geophysical Research*, 97(A6),
- 735 8319. doi: 10.1029/92JA00312
- 736 Shue, J.-H., Song, P., Russell, C. T., Steinberg, J. T., Chao, J. K., Zastenker, G., ...
- 737 Kawano, H. (1998). Magnetopause location under extreme solar wind condi-
- 738 tions. *Journal of Geophysical Research: Space Physics*, 103(A8), 17691–17700.
- 739 doi: 10.1029/98ja01103
- 740 Sperveslage, K., Neubauer, F. M., Baumgärtel, K., & Ness, N. F. (2000). Mag-
- 741 netic holes in the solar wind between 0.3 AU and 17 AU. *Nonlinear Processes*
- 742 *in Geophysics*, 7(3/4), 191–200. doi: 10.5194/npg-7-191-2000
- 743 Spreiter, J. R., Summers, A. L., & Alksne, A. Y. (1966). Hydromagnetic flow around
- 744 the magnetosphere. *Planetary and Space Science*, 14(3), 223–253. doi: 10
- 745 .1016/0032-0633(66)90124-3
- 746 Stone, E. C., Frandsen, A. M., Mewaldt, R. A., Christian, E. R., Margolies, D.,
- 747 Ormes, J. F., & Snow, F. (1998). The advanced composition explorer. *Space*
- 748 *Science Reviews*, 86(1-4), 1–22. doi: 10.1007/978-94-011-4762-0{_}1
- 749 Trattner, K. J., Burch, J. L., Ergun, R., Fuselier, S. A., Gomez, R. G., Grimes,
- 750 E. W., ... Young, D. T. (2016). The response time of the magnetopause
- 751 reconnection location to changes in the solar wind: MMS case study. *Geophys-*
- 752 *ical Research Letters*, 43(10), 4673–4682. doi: 10.1002/2016GL068554
- 753 Trattner, K. J., Burch, J. L., Fuselier, S. A., Petrinec, S. M., & Vines, S. K. (2020).
- 754 The 18 November 2015 Magnetopause Crossing: The GEM Dayside Kinetic
- 755 Challenge Event Observed by MMS/HPCA. *Journal of Geophysical Research:*
- 756 *Space Physics*, 125(7). doi: 10.1029/2019JA027617
- 757 Trattner, K. J., Mulcock, J. S., Petrinec, S. M., & Fuselier, S. A. (2007). Prob-
- 758 ing the boundary between antiparallel and component reconnection during
- 759 southward interplanetary magnetic field conditions. *Journal of Geophysical*
- 760 *Research: Space Physics*, 112(8). doi: 10.1029/2007JA012270
- 761 Treumann, R. A., & Baumjohann, W. (2013). Collisionless magnetic reconnection in
- 762 space plasmas. *Frontiers in Physics*, 1. doi: 10.3389/fphy.2013.00031
- 763 Tsurutani, B. T., Lakhina, G. S., Verkhoglyadova, O. P., Echer, E., Guarnieri, F. L.,
- 764 Narita, Y., & Constantinescu, D. O. (2011, 2). Magnetosheath and heliosheath
- 765 mirror mode structures, interplanetary magnetic decreases, and linear mag-
- 766 netic decreases: Differences and distinguishing features. *Journal of Geophysical*
- 767 *Research: Space Physics*, 116(2). doi: 10.1029/2010JA015913
- 768 Turc, L., Escoubet, C. P., Fontaine, D., Kilpua, E. K., & Enestam, S. (2016).
- 769 Cone angle control of the interaction of magnetic clouds with the Earth's
- 770 bow shock. *Geophysical Research Letters*, 43(10), 4781–4789. doi:
- 771 10.1002/2016GL068818
- 772 Turc, L., Tarvus, V., Dimmock, A. P., Battarbee, M., Ganse, U., Johlander, A., ...
- 773 Palmroth, M. (2020, 10). Asymmetries in the Earth's dayside magnetosheath:
- 774 results from global hybrid-Vlasov simulations. *Annales Geophysicae*, 38(5),
- 775 1045–1062. doi: 10.5194/angeo-38-1045-2020

- 776 Turner, J. M., Burlaga, L. F., Ness, N. F., & Lemaire, J. F. (1977, 5). Magnetic
777 holes in the solar wind. *Journal of Geophysical Research*, *82*(13), 1921–1924.
778 doi: 10.1029/ja082i013p01921
- 779 Volwerk, M., Mautner, D., Simon Wedlund, C., Goetz, C., Plaschke, F., Karls-
780 son, T., ... Varsani, A. (2021). Statistical study of linear magnetic
781 hole structures near Earth. *Annales Geophysicae*, *39*(1), 239–253. doi:
782 10.5194/angeo-39-239-2021
- 783 Wang, G. Q., Volwerk, M., Xiao, S. D., Wu, M. Y., Hao, Y. F., Liu, L. J., ...
784 Zhang, T. L. (2020, 11). Three-dimensional Geometry of the Electron-scale
785 Magnetic Hole in the Solar Wind. *The Astrophysical Journal Letters*, *904*(1),
786 L11. doi: 10.3847/2041-8213/abc553
- 787 Webster, L., Vainchtein, D., & Artemyev, A. (2021). Solar Wind Discontinuity
788 Interaction with the Bow Shock: Current Density Growth and Dawn-Dusk
789 Asymmetry. *Solar Physics*, *296*(6), 87. doi: 10.1007/s11207-021-01824-2
- 790 Yamada, M., Kulsrud, R., & Ji, H. (2010). Magnetic reconnection. *Reviews of Mod-
791 ern Physics*, *82*(1), 603–664. doi: 10.1103/RevModPhys.82.603
- 792 Yao, S. T., Wang, X. G., Shi, Q. Q., Pitkänen, T., Hamrin, M., Yao, Z. H., ... Liu,
793 J. (2017). Observations of kinetic-size magnetic holes in the magnetosheath.
794 *Journal of Geophysical Research: Space Physics*, *122*(2), 1990–2000. doi:
795 10.1002/2016JA023858
- 796 Zhang, H., Zong, Q. G., Sibeck, D. G., Fritz, T. A., McFadden, J. P., Glassmeier,
797 K. H., & Larson, D. (2009). Dynamic motion of the bow shock and the mag-
798 netopause observed by THEMIS spacecraft. *Journal of Geophysical Research:
799 Space Physics*, *114*(1). doi: 10.1029/2008JA013488
- 800 Zweibel, E. G., & Yamada, M. (2016). Perspectives on magnetic reconnection.
801 *Proceedings of the Royal Society A: Mathematical, Physical and Engineering
802 Sciences*, *472*(2196), 20160479. doi: 10.1098/rspa.2016.0479